Available online at www.sciencedirect.com
SCIENCE DIRECT®
Journal of Nuclear Materials 324 (2004) 140–151
journal of nuclear materials
www.elsevier.com/locate/jnucmat

Dynamic strain aging and grain size reduction effects on the fatigue resistance of SA533B3 steels

J.Y. Huang [a,b], J.R. Hwang [a,*], J.J. Yeh [b], C.Y. Chen [b], R.C. Kuo [b], J.G. Huang [c]

[a] Department of Mechanical Engineering, National Central University, Chung-Li 320, Taiwan, ROC
[b] Institute of Nuclear Energy Research (INER), P.O. Box 3-14, 1000 Wenhua Road, Chiaan Village, Lungtan 325, Taiwan, ROC
[c] Nuclear Operation Department, Taiwan Power Company, Taipei 325, Taiwan, ROC

Received 15 October 2002; accepted 13 September 2003

Abstract

Constant amplitude axial fatigue tests were conducted on SA533B3 steels with four levels of sulfur content at room temperature and 300 °C. Fatigue life was significantly affected by the inclusions. Fractographic examination results suggested that inclusions near the specimen surface served as the crack initiation site for a majority of the fatigued specimens tested at room temperature and that for those tested at 300 °C, some cracks were identified to initiate around the inclusions even in the interior of the fatigued specimens. Under the cyclic deformation, the dynamic strain aging (DSA) prevailed in the first few cycles at 300 °C, then the interactions among dislocations became dominant. Carbide or nitride precipitation in SA533B3 steels was enhanced synergistically by thermal energy and mechanical stress. It was shown that the combined effects of DSA and grain size reduction are responsible for the better fatigue resistance of SA533B3 steel at 300 °C.

PACS: 61.72.Ff; 61.72.Qq; 62.20.Fe; 62.20.Mk

1. Introduction

SA533B3 steel is the material most commonly used for nuclear reactor pressure vessels (RPV) whose integrity governs the safety of nuclear power plants. Fatigue is one of the main degradation mechanisms affecting the pressure vessel integrity of pressurized water reactors (PWR) and boiling water reactors (BWR) [1–10]. The most significant metallurgical variables affecting fatigue strength are manufacturing defects. Inclusions in steels, particularly sulfides, serve as crack initiation sites and sources of enhanced crack growth rates [2,3,11–13]. The nuclear plants were built in different periods of time. In the early stage little attention was paid to the sulfur content in the manufacturing of steels [14,15]. In the past 30 years, low-cycle fatigue behavior of the pressure vessel steels in high-temperature and high-pressure water environments was extensively studied [16–18]. Corrosion fatigue was generally performed under the conditions of low frequency and slow strain rate. The low frequency or slow strain rate provided a long-term interaction between sulfides and the water environment that would shorten the fatigue life of pressure vessel steel [17]. However, little work has been done to study the high-cycle fatigue behavior of RPV steel. Cyclic deformation in this study was conducted at a relatively higher strain rate than that for corrosion fatigue. To investigate the effect of sulfide on cyclic deformation behavior at room temperature and 300 °C, reactor pressure vessel steels, SA533B3, with four levels of sulfur content, were studied. In this paper, fatigue behavior was investigated in air. The effects of water chemistry environment and

* Corresponding author. Tel.: +886-3 426 7314; fax: +886-3 422 8550.
E-mail address: jrhwang@cc.ncu.edu.tw (J.R. Hwang).

0022-3115/$ - see front matter © 2003 Elsevier B.V. All rights reserved.
doi:10.1016/j.jnucmat.2003.09.009

cycling frequency on fatigue performance will be investigated and reported in subsequent papers.

Light water reactor pressure vessels are operated at about 300 °C, where carbon atoms in the steel matrix can interact with dislocations to form Cottrell atmospheres. Dynamic strain aging is the phenomenon commonly observed with low carbon alloy steels at a temperature range from 150 to 340 °C [19–23]. The dynamic strain aging phenomena are characterized with the increase of strength, reduction of ductility and discontinuous yielding during the serrated flow known as the Portevin–Le Chaterlier effect. The higher fatigue resistance of SA508 class 3 steel tested under the low-cycle fatigue conditions at 300 °C has been accounted for by the dynamic strain aging effect [19]. The strain rate for high-cycle fatigue testing is generally higher than that for low-cycle fatigue. Does dynamic strain aging still have an effect on the high-cycle fatigue resistance of SA533B3 steels? A microstructural evolution, with scanning electron microscopy (SEM) and transmission electron microscopy (TEM), has been studied to account for the improved fatigue resistance of SA533B3 steels tested at 300 °C than those tested at different temperatures.

2. Experimental procedures

2.1. Materials

SA533B3 steel plates with four sulfur content levels ranging from 0.006 to 0.034 wt% were manufactured by the China Steel Corporation according to the specifications of ASTM A533. The materials were rolled from a thickness of 150 to 13 mm and solution treated at 900 °C for 1 h, then quenched and tempered at 670 °C for 1 h. Their chemical compositions and mechanical properties are given in Tables 1 and 2, respectively.

2.2. Metallographic and fractographic examinations

To reveal MnS morphology and precipitates distribution, the as-received and fatigued specimens were polished following standard metallographic practice,

Table 1
Chemical compositions of SA533B3 steels

Designation	Composition (wt%)										
	C	Si	Mn	P	S	Ni	Mo	A1	N	Cu	Fe
I1	0.207	0.22	1.28	<0.02	0.006	0.61	0.52	0.015	0.005	0.03	Balance
I2	0.203	0.23	1.34	<0.02	0.015	0.50	0.53	0.015	0.005	0.01	Balance
I3	0.200	0.22	1.29	<0.02	0.027	0.62	0.51	0.013	0.005	0.04	Balance
I4	0.214	0.22	1.29	<0.02	0.035	0.61	0.51	0.012	0.005	<0.05	Balance

Solution treated at 900 °C for 1 h, then quenched and tempered at 670 °C for 1 h.

Table 2
Mechanical properties of SA533B3 steels

Designation	Temperature (°C)	Ultimate tensile strength (MPa)	Yield strength (MPa)	Total elongation (%)	Uniform elongation (%)	Charpy energy (J)	
						−40 °C	−60 °C
I1	25	722.0 ± 2.7	650.0 ± 0.0	29.5 ± 0.2	10.2 ± 0.3	103	69
	150	718.5 ± 1.5	632.5 ± 2.5	22.0 ± 0.2	7.6 ± 0.4		
	300	751.5 ± 0.5	600.0 ± 0.0	30.2 ± 0.2	11.0 ± 0.2		
	400	665.8	546	29.2	7.9		
I2	25	715.6 ± 0	645.0 ± 5.0	29.0 ± 0.1	10.2 ± 0.1	49	43
	150	683	605	22.7	8.8		
	300	727.1	573.0	30.2	11.7		
	400	629.5	510	28.9	7.3		
I3	25	714.6 ± 4.6	640.0 ± 10.0	28.9 ± 0.1	9.7 ± 0.5	30	23
	150	690.0	618.0	19.6	7.9		
	300	740.0 ± 3.0	584 ± 4	28.7 ± 1.0	11.4 ± 0.2		
I4	25	722.1 ± 1.0	644.0 ± 11.0	28.1 ± 0.3	9.6 ± 0.3	31	23
	300	742.5	583	28.6	11.46		

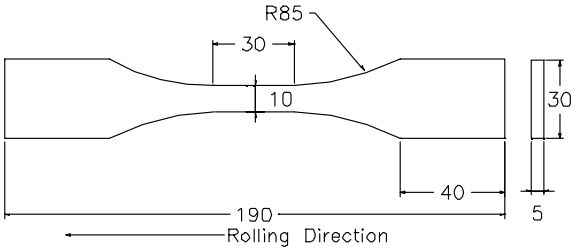

Fig. 1. Dimensions of the fatigue specimen.

then etched in a 5 vol.% Nital solution (5 vol.% nitric acid and 95 vol.% ethanol) for about 20 s and examined with optical and scanning electron microscopy. After fatigue tests, the fractured specimens were further investigated with scanning electron microscopy.

2.3. Cyclic deformation test

According to the ASTM E 466 specifications, plate-type fatigue specimens with a gauge length of 30 mm and thickness of 5 mm were manufactured, as shown in Fig. 1. Before fatigue testing, all specimens were well polished as per the recommendations of ASTM E 466. Constant amplitude axial fatigue tests at room temperature and 300 °C were performed with a 100 kN MTS 810 close-loop servohydraulic machine under a sinusoidal load control and at a load ratio R ($=\sigma_{min}/\sigma_{max}$) of 0.2, frequency of 20 Hz. The specimens were heated to 300 °C and then maintained for 2 h to homogenize the temperature distribution. The steel specimens were loaded in the rolling direction. Fatigue tests were stopped when specimens broke or the fatigue cycles reached 10^7 cycles. Based on test results [6], if a specimen could withstand the fatigue test to 10^7 cycles, it would last out the test well over 1×10^8 cycles. So, in this study, the fatigue strength at the level of 10^7 cycles was taken as the pseudo-fatigue limit.

2.4. Microhardness test

Vickers microhardness testing was conducted on the as-received, fatigued and tensile fractured specimens surface with different sulfur content levels. The hardness measurements were made at locations away from the necking region to avert the plastic deformation complications. The microhardness testing was performed at a deadweight of 300 g, loading speed of 100 μm/s and loading time of 10 s. The results were summarized in Table 3.

2.5. Transmission electron microscopic examination

To examine the fatigue effects on the evolution of the dislocation structure, TEM samples were cut from different locations along the fatigue-tested specimens with their sample surfaces normal and parallel to the loading axis, respectively. The TEM samples were polished with fine emery paper to a thickness of 0.1 mm, then chemically thinned with a double jet polishing machine in 10 vol.% perchloric acid ($HClO_4$) and 90 vol.% methanol (CH_3OH) at −30 °C. The current was controlled at approximately 0.1 A and voltage 10 V. The transmission electron microscope used in this study is a JOEL 2000FX operating at 200 kV.

3. Results and discussion

3.1. S–N curves

The S–N curves for SA533B3 steels with four levels of sulfur content at room temperature and 300 °C in air

Table 3
Microhardness (Vickers) of SA533B3 steels

Sample designation	Average Vickers hardness	G (ASTM grain size no.)	Average diameter (μm)
I1	218.6 ± 5.5	11.9	5.8
I2	217.6 ± 1.4	N.A.	N.A.
I3	214.7 ± 6.0	N.A.	N.A.
I4	222.4 ± 2.6	N.A.	N.A.
TI4U1	218.5 ± 3.0	13.4	3.5
HFI1 (669.5 MPa)	228.7 ± 2.1	13.3	3.6
HFI1 (682.5 MPa)	227.7 ± 2.1	N.A.	N.A.
THFI1 (650 MPa)	263.7 ± 4.0	N.A.	N.A.
THFI1 (669.5 MPa)	264.7 ± 5.4	13.8	3.0
THFI1 (682.5 MPa)	255.1 ± 4.0	N.A.	N.A.
Heat treated at 300 °C for 140 h	224.0 ± 5.4	12.9	4.1

I1, I2, I3, I4: As-received, TI4U1: tensile tested at 300 °C, HFI1: fatigue tested at room temperature, THFI1: fatigue tested at 300 °C applied maximum stress (σ_{max}) were noted in parentheses.

are shown in Fig. 2. The fatigue limit is observed around 650 MPa at room temperature. There is no significant difference between the S–N curves for the steels with various sulfur contents. The data were observed to scatter around the fatigue limit. At different stress levels, the standard deviations of the fatigue life for SA533B3 steels with four sulfur contents were calculated according to the conventional statistical equations.

Mean value of log-life:

$$\widehat{N} = \frac{1}{n}\sum_{j=1}^{n} \log N_j, \tag{1}$$

standard deviation of log-life:

$$\hat{\sigma} = \sqrt{\frac{1}{n-1}\sum_{j=1}^{n}(\log N_j - \widehat{N})^2}, \tag{2}$$

where n is the number of tests and N_j is the measured fatigue life.

Demonstrated below are the examples for SA533B3 steels at different stress levels.

$$\text{At } \sigma_{\max} = 682.5 \text{ MPa}, \quad \widehat{N} = 5.466, \quad \hat{\sigma} = 0.178 \tag{3}$$

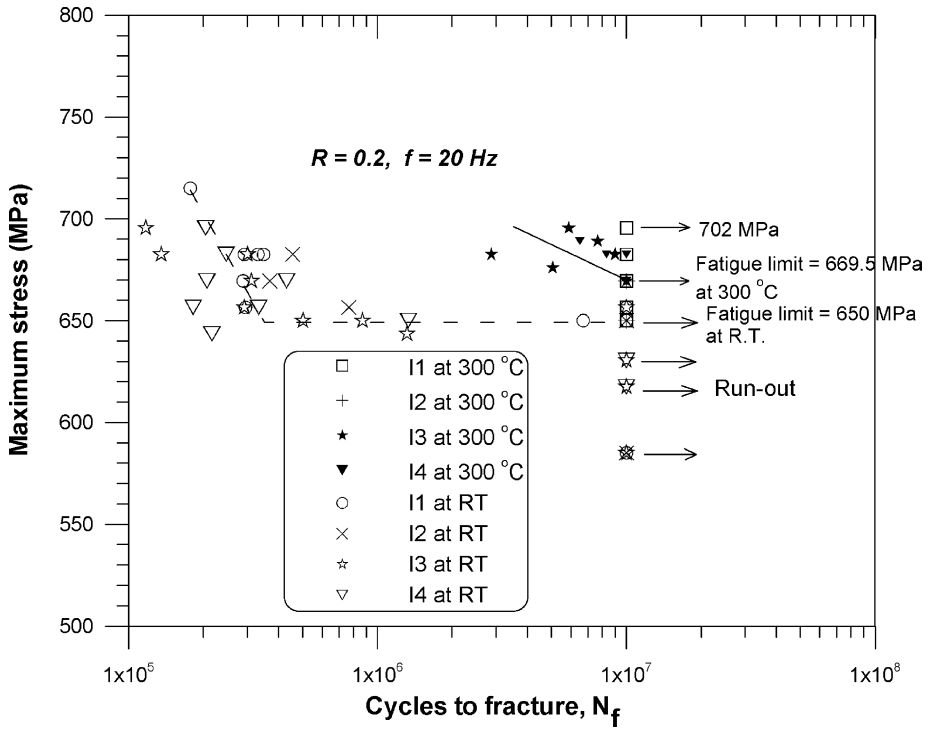

Fig. 2. S–N curves of SA533B3 steels with four sulfur content levels at room temperature and 300 °C.

Table 4
Effects of inclusions on fatigue life for SA533B3 steels

Sample no.	Frequency (Hz)	Maximum stress (MPa)	N_f (cycles)	Remark[a]
HFI2-4	20	650	354,297	w
HFI2-5	20	650	10 000 000	w/o
HFI3-15	20	656.5	292 051	w
HFI3-11	20	656.5	10 000 000	w/o
HFI4-3	20	656.5	181 873	w
HFI4-4	20	656.5	333 284	w/o
HFI4-2	20	669.5	206 071	w
HFI4-5	20	669.5	431 894	w/o

[a] w = with inclusions at the crack initiation site, w/o = without inclusions at the crack initiation site.

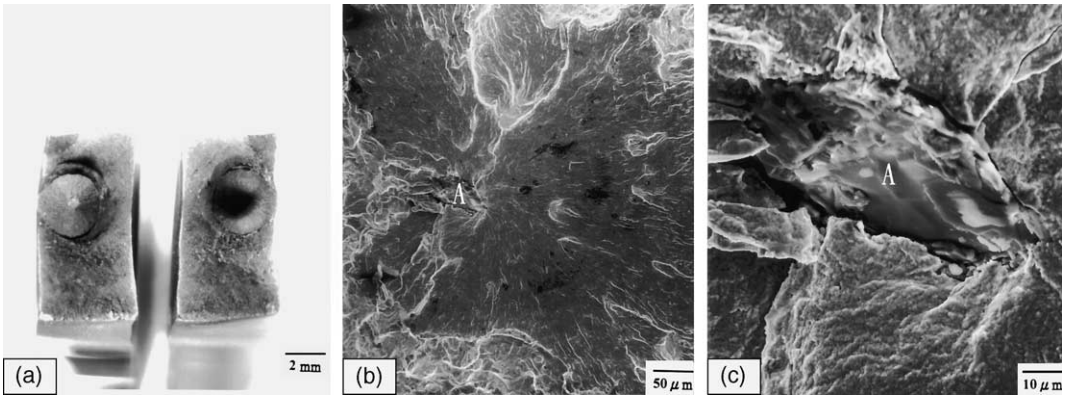

Fig. 3. Fatigue fracture surface of the I2 specimen at 300 °C: (a) overview of fracture surface, (b) fatigue crack initiated at inclusions and (c) inclusions at a higher magnification (A = inclusion).

and

$$\text{at } \sigma_{\max} = 656.5 \text{ MPa}, \quad \widehat{N} = 5.943, \quad \hat{\sigma} = 0.690. \qquad (4)$$

Apparently, the higher the maximum applied stress, the smaller the scatter of the fatigue life data. The reason why the fatigue life data are more scattered at low stress is that at lower stresses, the fatigue life is generally controlled by the crack initiation behavior. Crack initiation is very sensitive to the specimen surface conditions and the amount and distribution of inclusions [2,3,11,12], which could vary significantly from specimen to specimen, as shown in Table 4. At higher stresses, the fatigue life is greatly influenced by crack propagation characteristics, which are not sensitive to specimen variation. Therefore, the fatigue data at lower stresses are more scattered.

The fatigue limit for the R ratio of 0.2 is around the level of the yield strength. A small amount of plastic deformation was observed in the first few cycles [5,6], then became saturated till final rupture. The reduction of area for the unbroken fatigue-tested specimens is around 0–9%, which depends on the loading level. In this work, the applied stress, higher than the yield strength of the RPV steels, will induce strain hardening in the first few cycles. The yield point becomes higher with cyclic loading when the applied stress is higher than the yield strength due to strain hardening. After the first few cycles, the applied stress remains below the hardened yield strength and most of the fatigue cycles result in little plastic deformation. Thus, the fatigue life could last up to more than 10^5 cycles, which is the lower limit for high-cycle fatigue.

The fatigue limit for the steel with sulfur content higher than 0.006 wt% at 300 °C and the R ratio of 0.2 is around 669.5 MPa which is slightly higher than that tested at room temperature, 650 MPa. The fatigue limit for the steel with sulfur content 0.006 wt% is even higher, up to 702 MPa. This result suggests that the effect of sulfur content on fatigue life became saturated when the sulfur content is higher than 0.01 wt%, which is consistent with the corrosion fatigue behavior of the SA533B3 steel in the high-temperature and high-pressure water environment [10,16].

3.2. Effects of inclusions on fatigue life

Previous results show that inclusions have a deleterious effect on the fatigue life of steels [2,3]. SEM fractographs of the fatigued specimen at 300 °C, Fig. 3, indicate that the fatigue crack initiated around inclusions. The inclusions were randomly distributed in the interior of the specimen and around the surface. They were analyzed by the energy dispersive spectrum, EDS, to be composed of O, Al, S, Ca, P, and Mn, as shown in Fig. 4. Sulfur can easily react with Mn, Ca, Si, and Al to form hard, brittle compounds [24,25]. Over one hundred fatigued specimens were examined, the results show that no fatigue crack initiated at the inclusions of the specimens with a sulfur content level 0.006 wt%. It could be explained by the observations that the sulfide distribution becomes sparse and that the inclusions are relatively small when the sulfur content level is below 0.01 wt%, as demonstrated in Fig. 5. The results of Charpy impact tests also show that the Charpy energy drops dramatically when the sulfur content level is higher than 0.006 wt% and become saturated with sulfur content higher than 0.015 wt%, as shown in Table 2.

3.3. Dynamic strain aging, carbide/nitride precipitation and grain size reduction

The fatigue strength and fatigue limits of SA533B3 steels at 300 °C are apparently higher than those tested at room temperature. This could be due to the increase in the ultimate tensile strength at 300 °C, as listed in Table 2. The negative strain rate sensitivity was observed

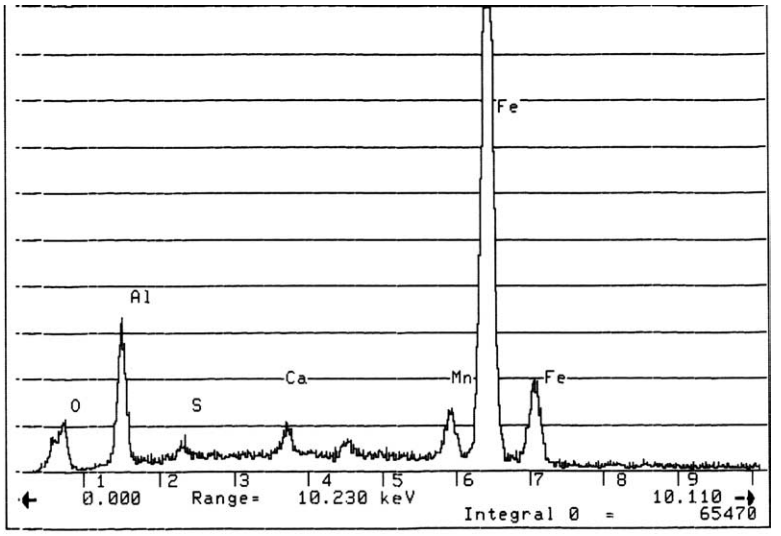

Fig. 4. Energy dispersive spectrum for the compositions of inclusion shown in Fig. 3.

at 150 and 300 °C, at which the tensile strength increased with decreasing strain rate, as shown in Fig. 6. Furthermore, the serrated flow was observed on the tensile stress–strain curve with strain rates of ~1–5×10^{-1} s^{-1} at 300 °C. It is well established that the negative strain rate sensitivity and serrated flow are the common characteristics of dynamic strain aging (DSA) [26,27]. Kim and coworkers [19,28] demonstrated that the dynamic strain aging would improve the low-cycle fatigue resistance and deteriorate the fracture toughness around 300 °C for the pressure vessel steel SA508 class 3. Mohan and Marschall [29] also reported that carbon steels, which are susceptible to dynamic strain aging, exhibit improved strength, creep resistance and fatigue resistance within the DSA temperature range. The phenomena of DSA are believed to be associated with the interactions between moving dislocations and solute atoms. Dynamic strain aging may occur when the diffusion rate of interstitial atoms keeps pace with the moving dislocations. The data in Table 2 were obtained

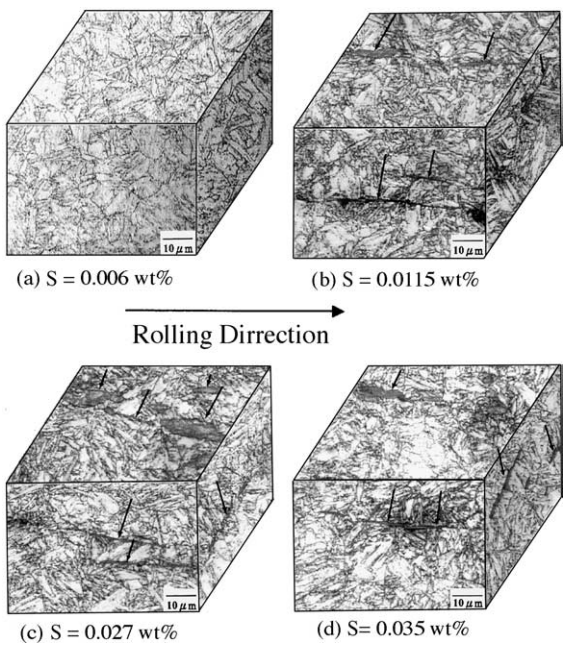

Fig. 5. Metallographs of SA533B3 steel with different sulfur contents: (a) I1, (b) I2, (c) I3, (d) I4 (the arrows indicate the sulfide).

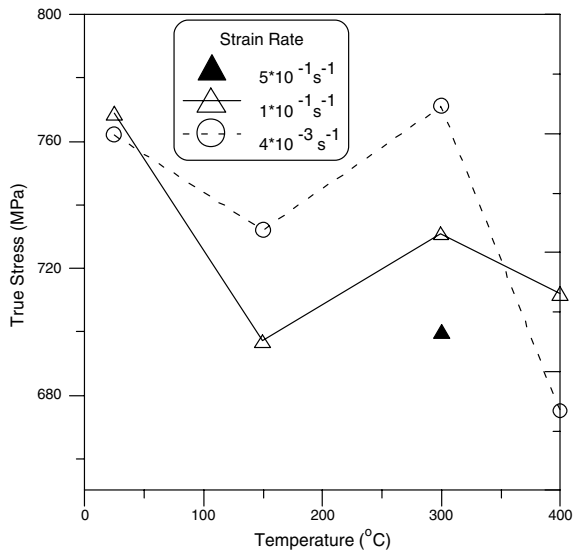

Fig. 6. Strain rate effects on the true stress at true strain 7% for I2 specimen.

at a nominal strain rate of 4×10^{-3} s^{-1}. It is reasonable that DSA occurs at such a strain rate [19,28]. But in this cyclic deformation, the strain rate measured using a high-temperature capacitance type extensometer was to be at $\sim1\times10^{-1}$ s^{-1} at 300 °C. At such a high strain rate, does DSA still occur and have effect on the fatigue resistance of SA533B3 steel? From Fig. 6, the negative strain rate sensitivity was observed at 300 °C, and the serrated flow was noted at the strain rate 1×10^{-1} s^{-1} for the monotonic loading. Serrated flow was also observed on the hysteresis stress–strain curves for the first 12 cycles of the fatigue tests at 300 °C, as exemplified in Fig. 7. After 12 cycles, the interactions between the solute atoms and the dislocations became saturated and cyclic stress induced multiple dislocations. The interactions between dislocations became dominant, thus serrated flow disappeared, as shown in Fig. 7(a) and (c). For the first 12 cycles, the additional strain increment was observed during unloading, as shown in Fig. 7(b). That could be accounted for by the dragging stress between the solute atoms and dislocations. The dislocations were dragged by the solute atoms during loading that resulted in different levels of dragging force upon the dislocations by the solute atoms. Under loading, the leading dislocations moved forward with smaller drag force than the dislocations following behind. Upon unloading, the leading dislocations kept moving forward because of the inertia, but the dislocations following behind reversed their moving direction by dragging force. Thus, a small strain increment was observed with each unloading on the hysteresis stress–strain curves. This result is consistent with those observed by Liaw and coworkers [5,6].

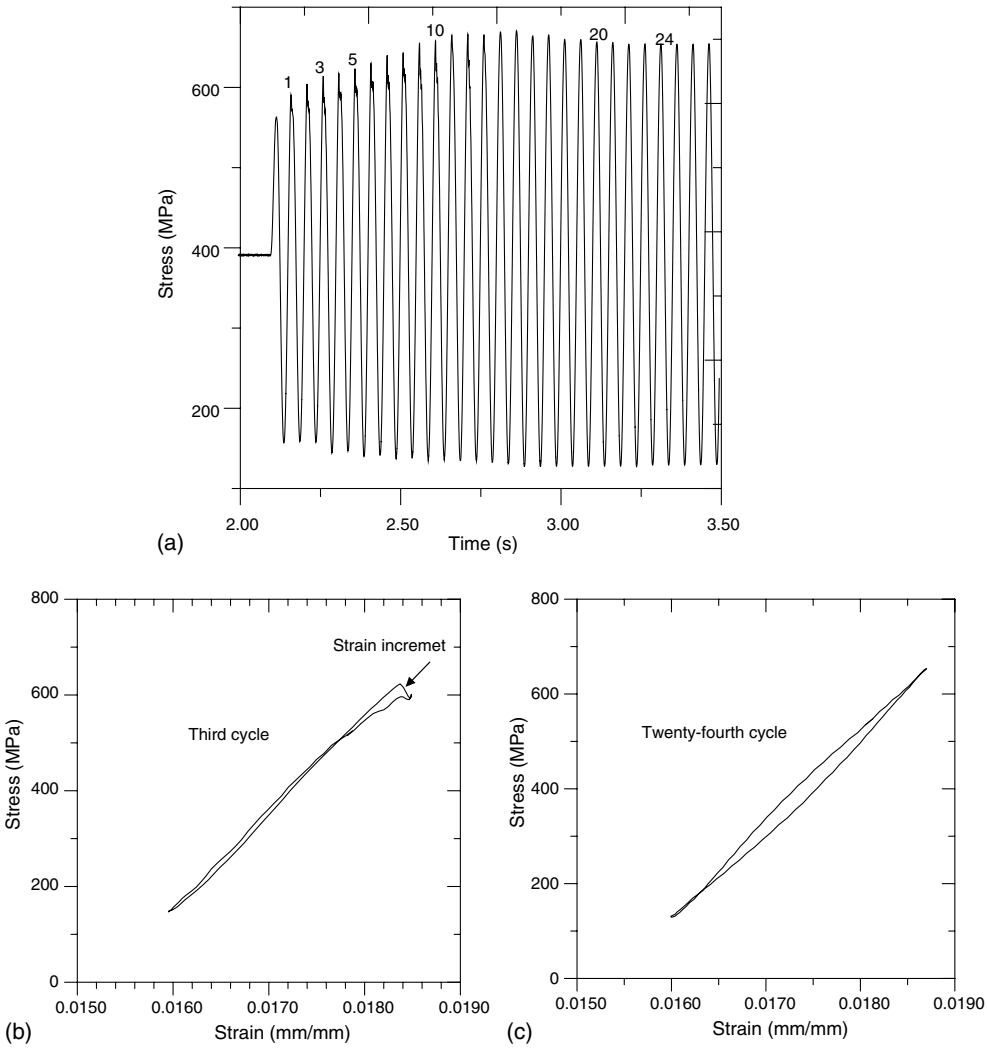

Fig. 7. Stress–time and hysteresis curves for I1 specimen at 300 °C: (a) stress–time curve, (b) hysteresis curve for the third cycle, and (c) hysteresis curve for the 24th cycle.

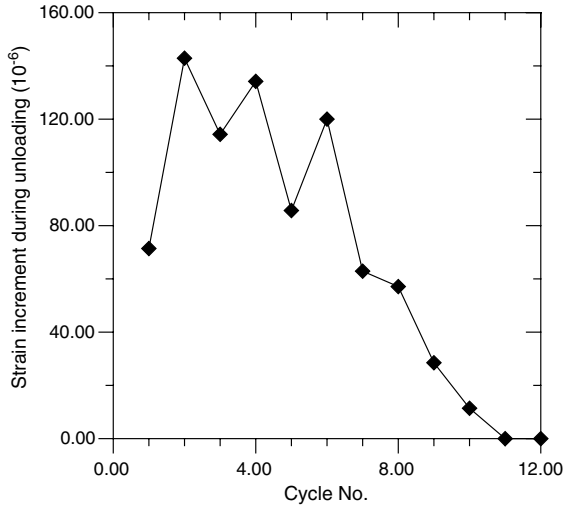

Fig. 8. Strain increment during the unloading of the first 12 cycles for I1 specimen fatigued at 300 °C.

The strain increment during unloading increased to larger values in the first 5 or 6 cycles and then decreased quickly with the fatigue cycles, as shown in Fig. 8. From the above discussion, it is believed that DSA indeed occurred in the first few cycles and could have effects on the fatigue resistance of SA533B3 steel at 300 °C.

In addition to the DSA effect on the fatigue resistance, microstructure examinations using SEM show that the carbide or nitride precipitation could play a role in the steel fatigue behavior, as shown in Fig. 9. The precipitation is much less significant in the as-received SA533B3 I1 steel specimen, Fig. 9(a), than those tensile tested at 150 and 300 °C, as illustrated in Fig. 9(b) and (c), respectively. Fatigue testing at 300 °C for 10^7 cycles induced more carbide or nitride precipitates and a significant reduction in grain size than tensile testing did, as demonstrated by a comparison of Fig. 9(b), (c) and 10(a). Which factor, temperature or mechanical stress or both, would have a more significant effect on the precipitation of SA533B3 I1 steel? The metallograph for the SA533B3 I1 steel specimen heat-treated at 300 °C for 140 h, which is equivalent to the elapse time of fatigue test for 10^7 cycles, was compared to those of the fatigued specimen at room temperature, as shown in Fig. 10(b) and (c). The precipitation did not increase significantly in both conditions. From Figs. 9 and 10, the precipitation of SA533B3 steels strongly depends on the synergistic effects of temperature (at 150 and 300 °C) and mechanical stress (static and cyclic). Thermal energy (at 300 °C) or mechanical stress alone would not enhance the precipitation significantly. However, the hardness of the specimens subjected to the fatigue test at 300 °C for 10^7 cycles indeed increased as shown in Table 3. Rao et al. [26] reported that the cyclic deformation enables the massive precipitation to proceed quickly because of the enhanced diffusion of solute elements with the aid of non-equilibrium vacancies generated during deformation. The precipitates of tempered martensite will decrease the strength of the steel. The precipitates in high-cycle fatigued SA533B3 steels also decrease the strength in a way similar to the tempering of martensite. The strengthening of martensitic steel is due to solution hardening, in which solute atoms (carbon or nitrogen) are trapped in the solid solution leading to lattice distortion. While carbides or nitrides precipitate at 300 °C, the strength naturally decreases as a result of the reduction of lattice distortion. But the grain size reduction generally increases the strength of the steel. Thus, the hardness as revealed in Table 3, is the combined effects of grain size reduction and carbide or nitride precipitation. From the above discussions, it could be inferred that the higher fatigue life for SA533B3 steel at 300 °C was the result of combined effects of DSA and grain size

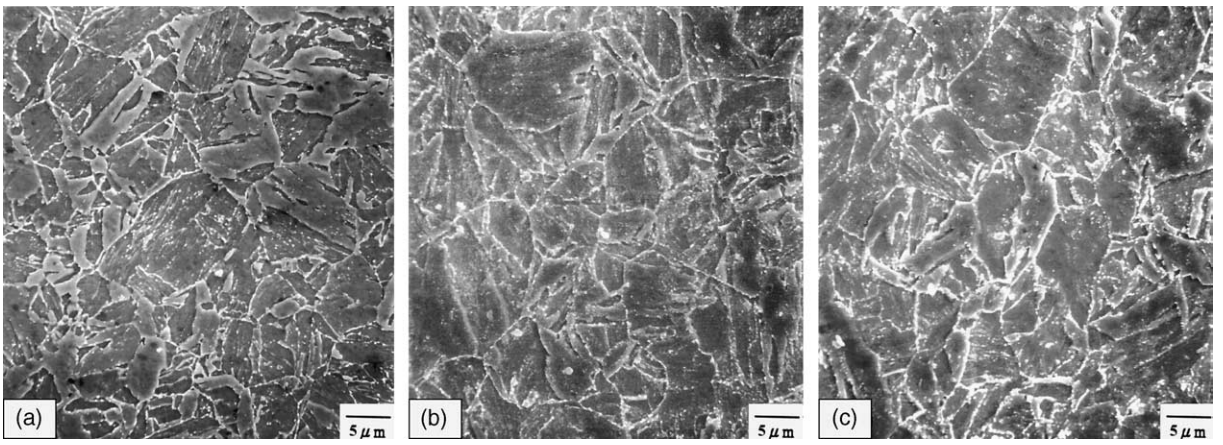

Fig. 9. Microstructural features of I1 specimen: (a) as-received, (b) tensile tested at 150 °C, and (c) tensile tested at 300 °C.

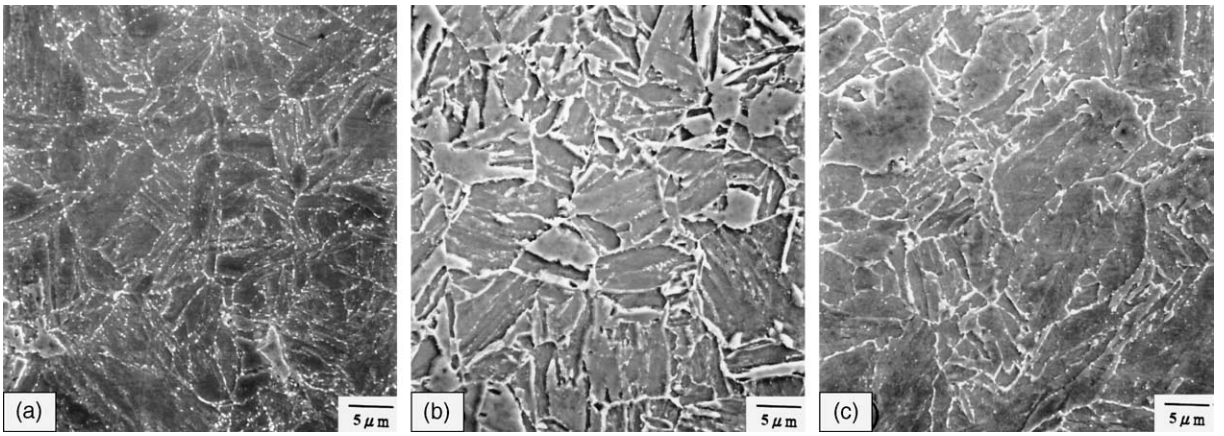

Fig. 10. Microstructural features of I1 specimen: (a) fatigue tested at 300 °C, (b) fatigue tested at room temperature, and (c) heat treated at 300 °C for 140 h.

reduction. The increased strength of SA533B3 steel, in turn, improved the fatigue limits for the specimens at 300 °C relative to those at room temperature.

3.4. Dislocation structure and sub-grain misorientation

A lot of researchers [3,11,30–36] have observed a strong dependence of dislocation structures on the fatigue test conditions. The fatigued specimens were examined by TEM and the misorientation between two neighboring sub-grains also analyzed. In order to prevent the final plastic deformation complicating the fatigue structure, the sampling positions should be as close to the final fracture site as possible, but kept away from the necking region. Fig. 11(a)–(d) are the TEM micrographs typical of the as-received and the fatigued specimens at room temperature, respectively. A significant number of particles were observed to precipitate along the sub-grain boundary and grain boundary. As with the observations made by scanning electron microscopy, precipitates were distributed along the grain boundary and in the interior of grains. Further details of the precipitates along the sub-grain boundary have been revealed through TEM examinations. No apparent distinction was found of the morphology of precipitates before and after fatigue tests at room temperature. This result is consistent with those observed by Fukuoka et al. [31]. However, the grains became smaller and elongated in their major axis after fatigue tested at 300 °C, as shown in Fig. 11(e) and (f), which is consistent with the SEM examinations as shown in Fig. 10(a) and also in good agreement with the higher hardness values summarized in Table 3. The cyclic loading at 300 °C induced numerous dislocations, dislocations tangling and polygonization as well as carbides/nitride precipitates at the sub-grain boundary and grain boundary. The sub-grain boundary became more discernible with the cyclic deformation through SEM examination, as shown in Fig. 10(a). That could be accounted for by the theory that the sub-grain boundary accommodated more dislocations, leading to the increase in the sub-grain boundary energy. The sub-grain boundary for the fatigue-tested specimens at 300 °C was easily etched in the Nital solution. The sub-grain boundary could be regarded as the grain boundary to impede the dislocation motion. The smaller grains improved the material strength and hardness, thus increasing the fatigue resistance.

Based on one-parameter selected area diffraction (SAD) examinations of the fatigued specimens, Fukuoka et al. [33] proposed that the misorientation, Θ, increases with fatigue damage accumulation even below the fatigue limit, exclusive of those tested at stresses lower than 50% of the fatigue limit. In this study, an SAD analysis, using a technique integrating Fukuoka's approach with the double-tilt method, was performed to evaluate the fatigue loading effects on the misorientation. Θ_x was determined by double exposure of the neighboring sub-grains at the same negative film. The double-tilt method was employed to examine the neighboring grains by adjusting Θ_y and Θ_z till both sub-grains displayed the same zone axis and symmetrical diffraction pattern, as illustrated in Fig. 12. Misorientation was then calculated by a three-dimensional formula of $\sqrt{\Theta_x^2+\Theta_y^2+\Theta_z^2}$. In this work, the misorientation ranges from 1 to 5°. From TEM results, it is very difficult to tell any distinction of misorientation before and after fatigue tests, although misorientation increases with the grain boundary energy [37]. There are a large number of precipitates inhomogeneously distributed in the grain boundary and sub-grain boundary of SA533B3 specimens. Complicated defect structures of precipitates, dislocations, dislocation cells

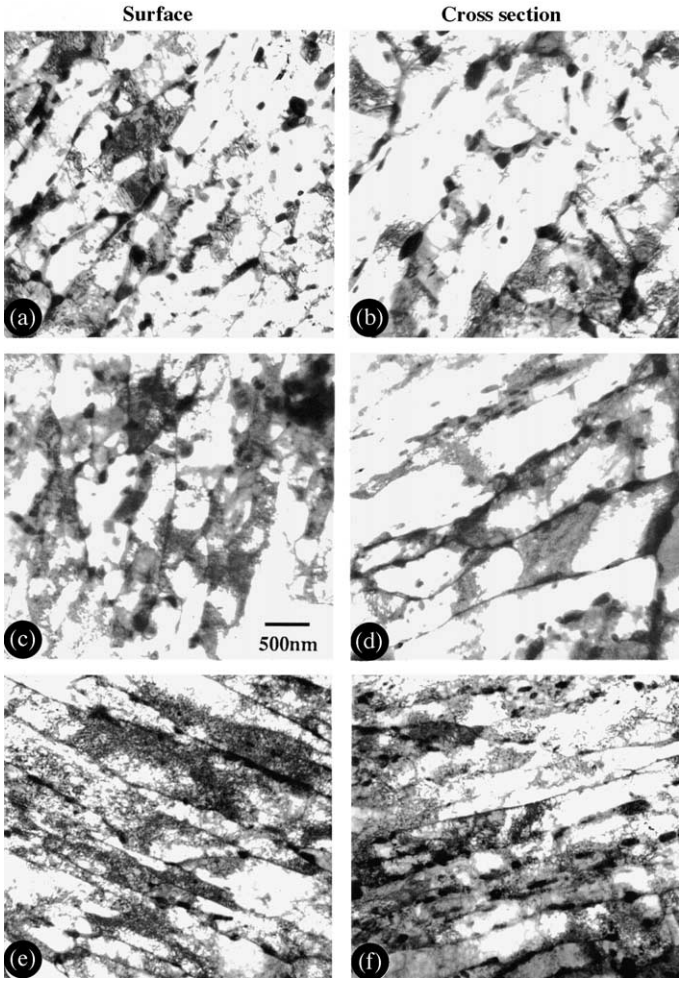

Fig. 11. TEM images of SA533B3 showing sub-grain structures in (a) and (b) as-received specimens, (c) and (d) fatigued specimens with $\sigma_{max} = 682.5$ MPa at room temperature and (e) and (f) fatigued specimens with $\sigma_{max} = 669.5$ MPa at 300 °C (all the scales are the same).

and sub-grains were observed to be prevalent in both the as-received and fatigued specimens. Currently, there is no general theory/model available to account for the observed defect structures.

4. Conclusions

(1) At room temperature, the fatigue limit for the SA533B3 steels was observed to be 650 MPa, around the yield strength and showed little or no dependence on sulfur content. At 300 °C, the fatigue strength and fatigue limit (669.5 MPa) was higher than those tested at room temperature, specifically the fatigue limit for the SA533B3 steel with a sulfur content 0.006 wt% is even higher, up to 702 MPa.

(2) Fatigue life is significantly affected by the inclusions which are composed of O, Al, S, Ca, and Mn. The inclusions were randomly distributed either on the surface or in the interior of the specimen. A great number of fatigue specimens tested at room temperature show that the fatigue cracks initiated at the sites of inclusions. At 300 °C, the crack were observed to initiate at the inclusions even in the interior of the specimen.

(3) Fatigue resistance of SA533B3 steel at 300 °C was improved by the combined effects of dynamic strain aging (DSA) and grain size reduction.

(4) Thermal energy and mechanical stress synergistically enhanced the precipitation of SA533B3 steel. A great number of precipitates were found distributed along the sub-grain boundary. There was no or little change of the morphology of precipitates before and after fatigue tests at room temperature, but the grains became smaller and elongated in their major axis of the fatigued specimens at 300 °C. The misorientation between two neighboring sub-grains ranges from 1 to 5°,

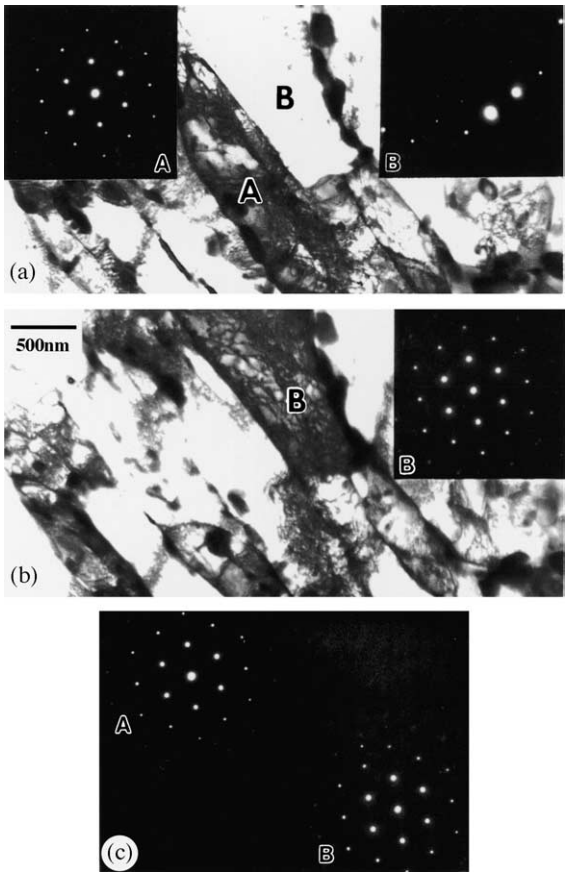

Fig. 12. Demonstration experiments showing the procedures of measuring three angular deviations (Θ_y, Θ_z and Θ_x): (a) TEM bright-field image with inset diffraction patterns showing grain A very close to zone axis, while grain B close to [1 1 1] zone axis. (b) TEM bright-field image after tilting grain B through Θ_y and Θ_z to the beam direction very close to [1 1 1] zone axis. (c) Superimposed diffraction patterns (very close to [1 1 1] zone axis) from grain A and grain B for measuring Θ_x.

bears no obvious relation to the accumulated fatigue damage.

Acknowledgements

The authors would like to acknowledge the financial support provided by the Taiwan Power Company.

References

[1] V.N. Shah, P.E. Macdonald, Aging and Life Extension of Major Light Water Reactor Components, Elsevier, 1993.
[2] J.Y. Huang, R.Z. Li, K.F. Chien, R.C. Kuo, P.K. Liaw, B. Yang, J.G. Huang, in: R. Chona (Ed.), Fatigue and Fracture Mechanics, vol. 32, ASTM STP 1406, 2001, p. 105.
[3] J.Y. Huang, C.Y. Chen, K.F. Chien, R.C. Kuo, P.K. Liaw, J.G. Huang, in: Proceedings of Julia Weertman Symposium, TMS Fall Meeting, 31 October–4 November 1999, p. 373.
[4] H. Nakajima, N. Nakajima, T. Kondo, in: Proceedings of a Symposium on Nuclear Power Plant Life Extension, Paris, 24–27 February 1987, p. 81.
[5] B. Yang, P.K. Liaw, J.Y. Huang, R.C. Kuo, J.G. Huang, Mater. Sci. Eng. A 314 (2001) 131.
[6] P.K. Liaw, H. Wang, L. Jiang, B. Yang, J.Y. Huang, R.C. Kuo, J.G. Huang, Scr. Mater. 42 (2000) 389.
[7] P.K. Liaw, W.A. Logsdon, J. Eng. Mater. Technol. ASME 107 (1985) 26.
[8] P.K. Liaw, C.Y. Yang, S.S. Palusamy, W. Ren, Eng. Fract. Mech. 57 (1997) 58.
[9] W.A. Logsdon, P.K. Liaw, Eng. Fract. Mech. 22 (1985) 509.
[10] J.M. Keisler, O.K. Chopra, W.J. Shack, Nucl. Eng. Des. 167 (1996) 129.
[11] M. Klesnil, P. Lukáš, Fatigue of Metallic Materials, Elsevier, Amsterdam, Netherlands, 1980.
[12] W.A. Van Der Sluys, W.H. Cullen, in: R Rungta, J.D. Gilman, W.H. Bamford (Eds.), Performance and Evaluation of Light Water Reactor Pressure Vessels, ASME, PVP-vol. 119, 1987, p. 63.
[13] C. Bathias, in: J.C. Newman Jr., R.S. Piascik, (Eds.), Fatigue Crack Growth Thresholds, Endurance Limits and Design, ASTM STP 1372, 2000, p. 135.
[14] K.E. Stahlkopf, J.D. Gilman, T.U. Marstan, in: R. Rungta, J.D. Gilman, W.H. Bamford (Eds.), Performance and Evaluation of Light Water Reactor Pressure Vessels, ASME, PVP-vol. 119, 1987, p. 1.
[15] W. Oldfield et al., Nuclear plant irradiated steel handbook, Report EPRI-NP-4797, 1986.
[16] O.K. Chopra, W.J. Shack, Effects of LWR coolant environments on fatigue design curves of carbon and low-alloy steels, Report NUREG/CR-6583, ANL-97/18, 1998.
[17] T. Kondo, J. Nucl. Sci. Technol. 26 (1989) 126.
[18] W.H. Bamford, J. Press. Vess. Technol. 102 (1980) 433.
[19] B.H. Lee, I.S. Kim, J. Nucl. Mater. 226 (1995) 216.
[20] D.V. Wilson, Met. Sci. (1977) 321.
[21] D.V. Wilson, J.K. Tromans, Acta Metall. 18 (1970) 1197.
[22] D.V. Wilson, Acta Metall. 21 (1973) 673.
[23] B. Mintz, D.V. Wilson, Acta Metall. 13 (1965) 947.
[24] W.C. Leslie, The Physical Metallurgy of Steels, McGraw-Hill, 1981.
[25] T.J. Baker, in: J.J. de Barbadillo, E. Snape (Eds.), Sulfide Inclusions in Steel, American Society for Metals, 1977, p. 135.
[26] K.B.S. Rao, M.G. Castelli, G.P. Allen, J.R. Ellis, Metall. Mater. Trans. A 28 (1997) 347.
[27] M. Valsan, D.H. Sastry, K.B.S. Rao, S.L. Mannan, Metall. Mater. Trans. A 25 (1994) 159.
[28] S.S. Kang, I.S. Kim, Nucl. Technol. 97 (1992) 336.
[29] R. Mohan, C. Marschall, Acta Mater. 46 (1998) 1933.
[30] C.Y. Chen, J.Y. Huang, J.J. Yeh, R.C. Kuo, J.R. Hwang, J.G. Huang, J. Mater. Sci. 38 (2003) 817.

[31] C. Fukuoka, H. Yoshizawa, Y.G. Nakagawa, M.E. Lapides, Metall. Trans. A 24 (1993) 2209.
[32] C. Laird, Metall. Trans. A 8 (A) (1977) 851.
[33] C. Fukuoka, Y.G. Nakagawa, Scr. Mater. 34 (9) (1996) 1497.
[34] K. Katagiri, A. Omura, K. Koyanagi, et al., Metall. Trans. A 8 (A) (1977) 1769.
[35] D. Kuhlmann-Wilsdorf, C. Laird, J. Mater. Sci. Eng. 27 (1977) 137.
[36] J. Awatani, K. Katagiri, H. Nakai, Metall. Trans. A 9 (A) (1978) 111.
[37] M.A. Meyers, K.K. Chawla, Mechanical Metallurgy, Prentice-Hall, New Jersey, USA, 1984, p. 276.